Comprehensive Geophysical study at Wabar crater, Rub Al-Khali desert, Saudi Arabia

Sherif M. Hanafy[1], Pantelis Soupios[1], Alexandros Stampolidis[2], Christian B. Koch[3], Khalid Al-Ramadan[1], Abdullatif Al-Shuhail[1], Theis Solling[1], and Ignatius Argadestya[1]

[1]King Fahd University of Petroleum and Minerals, College of Petroleum Engineering and Geosciences, Dhahran. Saudi Arabia

[2]School of Geology, Aristotle University of Thessaloniki, Greece

[3]University of Copenhagen, Department of Chemistry, Denmark

Key Points:

- To investigate the possibility of any major pieces of the meteorite remaining in the crater site, which we proved to be negative
- To investigate the meteorite direction
- To map the deformation structures associated with meteorite impacts and Wabar in particular

Corresponding author: Sherif M. Hanafy, `sherif.geo@gmail.com`

Abstract

The study of impact craters on Earth has picked up high worldwide consideration, which can be done by studying the ground surface using remote sensing (satellite), geological outcrops, drilling holes and apply small-scale laboratory experiments trying to build the dynamic models of crater formation and by collecting geophysical data. In this work the near- crater sediments at the young Wabar crater field in Saudi Arabia has been investigated using the magnetic, EM, seismic, and GPR methods. The main targets of this research were exploring the possibility of any remnant major pieces of the meteorite, investigate the meteoroid direction, and map the deformation structure associate with the meteorite impact. Our results shows five different magnetic anomaly types and three layers at the subsurface. The maximum deformation due to the impact of the meteorite is about 25 m as shown by both the seismic traveltime tomogram and the 3D GPR model. Transient EM survey confirmed the geometrical characteristics of the major crater and locate a smaller crater (known as Philby-A). The magnetic survey shows no evidence of any major piece of the meteorite, however, it was used to trace ejecta material containing highly dilute magnetic material. The magnetic carrier is most likely spheres of metal incorporated in the black/green glasses. During the expedition, many small pieces of the meteoroid were found and collected for further geochemical analysis. Based on the geophysical findings, the meteorite direction was found to be from north to south.

Plain Language Summary

In this study, we used magnetic, EM, seismic, and GPR methods to explore the subsurface at the Wabar meteoroid impact site. This site is located at the empty quarter (Rub Al-Khali) area, southeast of Saudi Arabia, where a large piece of the meteoroid was found and moved to the British Museum in the 1930s. The geophysical readings was processed and interpreted to create a subsurface model of the impact area and the surroundings to investigate the possibility of any major pieces of the meteorite remaining in the crater site, investigate the meteorite direction, and map the deformation structures associated with meteorite impacts and Wabar in particular.

1 Introduction

Meteorite impacts have been established as an important geological process shaping the surfaces of planetary bodies at various length and time scales (Osinski & Pierazzo, 2013). Currently, 190 impact structures are confirmed on Earth (Earth Impact Database, http://www.passc.net, 2020). These, together with extraterrestrial structures, constitute the ground truth end product regarding various aspects of the impact process, and have been instrumental in establishing dynamic details of the complex impact processes (Osinski & Pierazzo, 2013).

The typical hypervelocity impact induce the formation of a crater involving a depression lined by strongly modified rock/sediment and partially back filled with impact melt rock and impact breccias and a raised rim at the crater edge. The contrasting physical properties of the pre- and post-impact structure and materials make geophysical methods applicable to studies of the crater.

The Wabar crater field is a group of three closely spaced (rim diameters 114 m for Philby-B, 64 m for Philby-A, and 11 m) very young impact craters formed by impact of an iron meteorite (type IIIAB) into mostly loose quartz-dominated sand dunes in the desert of Rub Al-Khali (Empty Quarter), Saudi Arabia. The Wabar craters were first described and surface mapped in 1932 and reported by (Philby, 1933a, 1933b) in collaboration with (Spencer, 1933; Spencer & Hey, 1933). The craters are situated within an active dune field causing both covering up and uncovering over time of the craters and fragments of the bolide. In the sixties a substantial piece of the meteorite was uncovered in the vicinity of the craters (Abercrombie, 1966), and in the nineties the 11-m crater was uncovered and reported (Wynn, 1996). Fragments of the meteorite and sharpnels (up to 10 cm) from the crater-forming meteors are expected to be distributed within and around the craters.

Thermolumine dating indicate an age less than 300 years combined with its setting in a relatively dry environment of Rub Al-Khali in Saudi Arabia makes it very attractive to studies of unmodified material formed in the impact. Currently, two of the craters are completely buried and the third one partially buried below an active dune field prohibiting ground based characterization.

The geophysical methods have been successfully used to study a number of impact craters (exposed or buried beneath postimpact sediments) by imaging the subsurface and obtaining information about the spatial and in-depth variations of different physical properties (e.g., seismic velocity, density, resistivity, magnetic, and dielectric susceptibility, etc.) (Jansa et al., 1989; Hildebrand et al., 1991; Grieve & Pilkington, 1996; Grieve, 2006).

Changes in these physical properties at shallow layers (impact/deformed zone) are good indicators of lithological changes that are usually associated with the formation of a crater providing a clear geophysical signature. A detailed review of the geophysical anomalies and their resolution, that can be observed at geophysical surveys conducted at impact craters, can be found in (Pilkington & Grieve, 1992; Grieve & Pilkington, 1996; Grieve, 2006).

Most geophysical methods can be used for impact crater exploration including potential field (gravity and magnetic), seismic (refraction, reflection), ground penetrating radar (GPR), geoelectrical (DC), and electromagnetic (EM) (magnetotelluric, EM34) methods (Morgan & Rebolledo-Vieyra, 2013). It should be mentioned that most of the information about the applicability and success of the proposed geophysical methods comes from large scale (100-1000 km) impact craters. At these scales the geophysical signature can be differentiated based on the area and the thickness of the deformed zone cover and the host lithological units. A short description of the different geophysical methods used for crater exploration and their resolution and geophysical signature, is given in the following section.

2 Geophysics and Meteoroids

The gravity data are sensitive to density changes observing positive (higher densities) and negative (lower densities) gravity anomalies, relative to a background value. (Pilkington & Grieve, 1992) show that an impact crater produces a circular gravity low (negative gravity anomalies) that extend out to and often beyond the crater rim (Grieve, 2006). The gravity low is caused by fracturing of the host rocks (bedrock) and the post-impact sedimentary infill (Grieve & Pilkington, 1996). Depending on the size of the impact zone, (100 kilometers at Manicouagan for example) a central gravity high, which is produced by a central uplift of denser material (the bedrock) can be observed (Sweeney, 1978).

Magnetic surveys, airborne or ground, measure the distribution of iron-rich ferromagnetic minerals in the crustal rocks. Their magnetization could be either induced or remanent. Meteorites, especially iron-meteorites, are similar to terrestrial rocks and exhibit magnetization. (Herndon & Rowe, 1974) presented an overview of magnetism in meteorites. Magnetic signatures of impact craters have been extensively studied by many researchers (Gilder et al., 2018; Neville et al., 2014).

The direct current (DC) data (geoelectrical tomography) are sensitive to porosity/permeability changes observing positive (higher resistivities at the central uplift) and negative (lower resistivities due to the impact breccias, fractured bedrock and basin infill) resistivity anomalies, relative to a background resistivity value. (Tong et al., 2010) applied geoelectrical profiling in the central part of the Araguainha impact structure in central Brazil and provided evidence to support the existing model in which the deposition and flow of impact melt and breccias over the central uplift were influenced by the geometry of the lithologic boundaries in the central uplift.

EM surveys, as DC methods, are sensitive to the electrical properties of the subsurface and are used to model the 1D, 2D, and 3D subsurface resistivity distribution. Usually resistivity decreases with increasing primary (due to pore space fluids in porous materials) or secondary (cracks filled with fluids) porosity. Thus, at impact craters, the resistivity is usually lower inside the crater except for the central area where a high resistivity anomaly is observed due to the uplift of massive rocks (Pohl et al., 1977).

Seismic refraction and reflection have been used to find the subsurface velocity models of impact sites (Pohl et al., 1977; Pilkington & Grieve, 1992). The seismic velocity values are usually decreased at impact craters due to the decrease in the density and increase of the porosity as a result of the fracturing that occurs after the impact. In some cases, especially in large craters, such as the Vredefort Dome in South Africa, high velocity could be observed at the center of the crater impact (Pretorius et al., 1986; Durrheim, 1986; Therriault et al., 1996; Henkel & Reimold, 1998; Tinker et al., 2002). Impact melt could explain the increase of seismic velocity (Barton et al., 2010), however, in some other cases, the impact melt could cause a decrease in the seismic velocity (Salisbury et al., 1994), which depends on the type of rock at the impact site.

Ground Penetrating Radar (GPR) surveys were not used a lot to investigate crater impact sites due to its limited depth of penetration, however, it was used in small-scale craters such as the Kamil crater in Egypt (Folco1 et al., 2010).

Concerning the resolution of the first three methods (gravity, magnetic, and geoelectric), it should be mentioned that all methods governed by Laplace's equation have an undefined resolution and can be considered as first-order approximations or as preliminary models. However, the last two methods (seismic and GPR) are considered medium- to high-resolution techniques (Morgan & Rebolledo-Vieyra, 2013).

The most recent of those impact events in Saudi Arabia is the Wabar Craters in the Rub Al-Khali desert (Figure 1). (Wynn, 2002a, 2002b) described the results of a ground magnetic survey over the area of the crater. They pointed out that just a tiny fraction of the iron-nickel meteorite was left in the known craters, but it is possible that raw meteorite material could be found in the area, hidden under the sand dunes.

In this work we use magnetic, transient electromagnetic method (TEM), seismic refraction, and GPR methods to investigate the subsurface geological setting at the Wabar impact crater site located in Rub Al-Khali area, Saudi Arabia. The main aims of the paper is to investigate the possibility of any major pieces of the meteorite remaining in the crater site, investigate the meteorite direction, and map the deformation structures associated with meteorite impacts and Wabar in particular.

3 Field Acquisition

The geophysical survey was conducted during two field campaigns, one during Dec. 2019 for 2 days and the second, during February 2020 for 2 days. During the first campaign, magnetic, TEM, Seismic and GPR data were acquired and during the second visit, the magnetic survey was extended to the West and South of the initial study area and more gridded Magnetic and GPR data were recorded focused on specific sites of interest determined from the preliminary processing of the geophysical data recorded during the first geophysical survey (Figure 2). A hand-held GPS Garmin was used to setup all geophysical surveys and all data and results were georeferenced using GIS. Ground elevations for topographic corrections is recorded with the magnetometer's GPS (total of 70,000 stations), its spatial accuracy is about 1-3 m while the elevation accuracy was much less.

3.1 Magnetic Method

The magnetic survey was done with a Geometrics G-858 Cesium Magnetometer configured as a gradiometer with two vertically separated sensors. The bottom sensor was placed at 0.4 m above ground, while the top sensor at 1.4 m. This allows the measurement of the vertical gradient independent of diurnal variations. Concurrently, a magnetic base station was set up to correct for the diurnal variations. Applying the diurnal corrections on both the bottom sensor and the top sensor allowed us to produce maps of the total magnetic field for both sensors.

The survey was acquired along almost parallel lines in N-S direction (Figure 2), at an average 15 m line spacing, while recording was continuous at 5 Hz (0.2 sec per station). Oversampling along lines made it possible to distinguish short-wavelength anomaly patterns that wouldn't be possible otherwise. The geomagnetic survey covered a total area of about 500 m x 500 m (Figure 2). The spatial positions of magnetic stations were determined using the magnetometer's GPS (the accuracy of which is limited to 1-3 m), while a hand-held GPS was also used. Data on both GPS were almost identical; therefore we use here the magnetometer's GPS data.

The first field season centered on the Philby-B impact crater (Figure 2), covering an area of 200 x 250 m. Due to the high magnetization of the Camel Hump iron meteorite, the survey was expected to locate strong magnetic anomalies related to buried segments of the meteorite. A total of 20,000 stations were recorded. Strong short-wavelength magnetic anomalies (>800 nT) at the northern rim of Philby-B were identified.

During the second fieldwork, those anomalies were confirmed to originated from iron bars buried in the sand from previous geophysical surveys in the broader study area. The surveyed area was extended to the west to cover a total of about 0.25 km^2. A total of additional 50,000 stations were recorded. Strong local anomalies were again recorded.

The data were corrected for diurnal variations, and then the International Geomagnetic Reference Field (IGRF 2015) was subtracted from them. Residual data were gridded, and leveling corrections were applied. Based on the size of the Philby-B crater (more than 100 m diameter) the grid spacing was set to 10 m. The resulting color-scale map representing the intensities of magnetic anomalies are shown in Figure 3. The gridded magnetic data are characterized by small field variations (a few tens of nT). These are in consistence with data ranges reported by (Wynn, 2002a; Prescott et al., 2004).

The gridded data were reduced to the north pole (RTP) and upward continued to 5 m to filter out the near-surface anomalies (Figure 3). Their magnetic anomalies exhibit a very narrow range of residual anomalies (about -4 to 4 nT).

On the other hand, magnetic signal along profiles contains details for the magnetic field anomalies that are lost through the gridding procedure. We noticed that they follow certain patterns that were divided in 5 classes (Figure 4). The classes division was based on the signal's amplitude and wavelength. In Figure 5 their spatial distribution is presented with different colors:

- Class A: Weak anomalies, medium wavelengths with amplitudes less than 6.8 nT
- Class B: Strong anomalies, medium wavelengths with amplitudes $\approx$ 16.8 nT
- Class C: Weak anomalies, short wavelengths with amplitudes $\approx$ 3.5 nT, extended along profile covering a broad area
- Class D: Weak anomalies, long wavelengths with amplitudes $\approx$ 6.9 nT
- Class E: High amplitude anomalies, short wavelengths with amplitudes $\approx$ 197.7 nT

The most striking features in Figures 3 and 4 are the weak magnetic anomalies of class C, that correlate very well with the ejecta fields, and the strong anomalies of class E. Part of them were excavated, close to the northern rim of Philby-B, and found to be rusted man made metal beams. The class C features follow a pattern similar to that described in (Urbini et al., 2012).

3.2 TEM Survey

As shown in Figure 2, eighteen TEM soundings were acquired along a profile running from northwest to southeast corners of the survy site. The decision to acquire TEM data along a NW-SE profile was based on a published paper by (Gnos et al., 2013) showing the locations (coordinates of the center) of Philby-A and Philby-B craters. Thus, we tried to collect all TEM sounding along one profile that pass over both craters trying to sample the area outside the craters (depth to the bedrock or thickness of sand-dune's layer) but also to reconstruct, if possible, the geometry (depth of deformed zone) of the craters.

Based on the literature but also the visual evidence (only for Philby-B using satellite images), the diameters of Philby-A and Philby-B, are 64 m and 114 m, respectively. Thus, we decided to acquire the 18 TEM soundings spaced every 20-30 m (total length of the TEM profile was 416 m) to be able to reconstruct with the highest accuracy, of both craters.

The TEM measurements were carried out using the ABEM-WalkTEM system developed by Aarhus University and promoted by GuidelineGeo Inc. A central square loop configuration with a single-turn (40 m side, loop area 1600 m^2) transmitter loop and one coil (0.5 m side square loop with 20 internally turns in the center of the transmitter loop, giving a total receiving area of 5 m^2) was used to receive the signal. To increase the signal to noise ratio (SNR), three cycles (stacks) of measurements over the same location was applied. An external 12V battery to power the whole system was used and an average current of 6.6 A was emitted.

The acquisition protocol used was the dual (low and high) moment 25 ms with 45 gates. The low moment is used for early-time gate measurements (near surface mapping), whereas the high moment is mainly applied for later-time gate measurements (characterization of the deeper layers). The total measuring time was 24,538 μs, divided into 45 gates where the shortest and longest gate is equal to 2 μs and 4,765 μs, respectively. At the time of measurements, the noise (natural background noise for both moments) is also recorded and used for determining the depth of investigation (DOI). Moreover, the study area was very remote and no other disturbances were found to affect significantly the signal.

The data can be plotted in different ways (but we selected the stacked apparent resistivity option). Filtering and denoising was applied automatically as soon as the data were imported to the software. The uncertainty for each data point can be changed based on the available a priori information. It should be mentioned that no a priori information for the study area is found. Any resulted inverse model can be used as a starting model for the next inversion process. The final processed data and inversion models are all saved in the same SPIA database and can be imported directly into Aarhus Workbench for easy visualization of the results. The data residual was around 0.88 but some sounding (those collected inside Philby-B, T12 and T13) have an average data residual equal to 2.2.

TEM data were processed and inverted using the Aarhus SPIA software. The final filtered data (Figure 6a) were inverted using the robust and fast AarhusInv inversion code applying different degree of smoothing (low, normal, or high). A resistivity model is calculated that fits within the error bars of every measurement point (Figure 6b). Due to inherent geophysical ambiguity, an infinite number of models can fit the data but if the error bars are small (data quality is high), most of the models that fit the data will be very similar and thereby more probable. Two different resistivity models are always calculated. A layered resistivity model (Figure 6d) where the best fit of the model is achieved with the minimum number of layers possible (assuming that the mean resistivity within a specific layer is correct). A smoothed resistivity model (Figure 6c) is also estimated assuming that the subsurface is consisting of 20 layers with increasing thickness with depth. In this way, smaller and gradual changes in resistivity are determined. In this survey, the Aarhus Workbench has been used for visualization of the TEM-data. A quasi-2D profile by interpolating the TEM soundings was created and presented under the results section.

3.3 TEM Results and Interpretation

During the processing of the TEM soundings, we noticed that the TEM data collected along a NW-SE profile did not responded in the same way (to have smooth change of resistivity with depth where the high moment data are complementary of the low moment data). Thus, we have decided to apply a qualitatively interpretation. The soundings can be divided into 5 clusters (N-no change, L-low changes, M-medium changes, M2H-medium-high changes, and H-high changes). These five clusters (shown with different colors) and their TEM responses (as depicted inside the dashed blue ellipse) are shown in Figure (7). Specifically, soundings T1 and T2 did not show any significant disturbance, since only the expected gradual resistivity change with depth is observed. In sounding T3, an anomaly was found (dashed circle) and continued to soundings T4 and T5 with higher amplitudes (for an almost 50 m along the profile). This anomaly area is associated to the Philby-A crater but is slightly shifted to the southeast.

Sounding T6 was not influenced by any subsurface anomaly structure and has the same pattern as T1 and T2. TEM soundings T7 to T10 show a low disturbance at TEM responses but this response changes to medium in T11 as the TEM soundings approach the Philby-B. Soundings T12 and T13 present the highest disturbance which agrees with the location of Philby-B as shown in Figure 7. The medium to high change is continued to soundings T14 to T17 and the response becomes smaller (medium) at the last sounding (T18). Based on the qualitative interpretation of the TEM responses, an asymmetry is observed showing that the deformed zone is mainly extended at the southeast part of the study area.

3.4 Seismic Refraction Method

One seismic profile is recorded at the area. The profile is running from the north (50.4725583 E, 21.504011 N) to the south (50.4724777 E, 21.5019 N) as shown in Figure 2. The total profile length is 235 m. A total of 48 receivers are used with receiver interval of 5 m, the first receiver is located at offset 0 m and the last receiver is located at offset 235 m. A total of 87 common shot gathers (CSG) are recorded with shot interval of 2.5 m, the first shot is located at receiver no. 5 (offset 20 m) and the last shot is located at receiver no. 48 (offset 235 m). Due to a problem with the trigger cable, shots between offset 0 and 17.5 m are skipped. Figure 9 shows a sample receiver gather, which shows a high signal-to-noise ratio first-arrival event.

The first arrival traveltimes of all recorded CSGs are picked using an in-house developed software. To evaluate the quality of picking we applied the reciprocity test to all picked data. Reciprocity test can be described as follow; assume that we have two points on the ground surface i and j with an offset x between them. If point i is a source and point j is a receiver, then the traveltime from i to j is given by τ_{ij}, and if point i is a receiver and point j is a source, then the travel time from j to i is given by τ_{ji}. According to the reciprocity principle, the travel time from i to j (τ_{ij}) should be equal to the traveltime from j to i (τ_{ji}) regardless of the complexity of the velocity model.

In this work and for practical reasons, we accepted any traveltime pairs that satisfy the condition

$$abs(\tau_{ij} - \tau_{ji}) \leq T/4. \tag{1}$$

where abs is the absolute value and T is the period of the first arrival wavelet. If the traveltime pairs (τ_{ij} and τ_{ji}) did not satisfy the reciprocity condition, then both traveltimes are rejected and excluded from the following processing steps.

Figure (10a) shows the travetime picking of the recorded data before the reciprocity test. The total number of picked traces is 4,176. Here, 1,008 traveltime picks (504 pairs) did not pass the reciprocity test, which means that about 24 % of the picked data are rejected. Hence, we repicked the rejected traces and we were able to decrease the number of rejected traces to 158 trace (79 pairs), which means that only 3.8 % of the picked traveltimes did not pass the reciprocity test. They are rejected and not included in the traveltime inversion process.

The picked traveltimes that passed the reciprocity test are inverted to generate the traveltime tomogram. One of the important inputs for the traveltime inversion algorithm is the initial velocity model. Since we have more shots than receivers, we used the picking of 3 common receiver gathers (CRG 5, 24, and 48) to generate a proper initial velocity model. The x-t curves of the selected CRGs shows that we have 3 different layers, the apparent velocity of each layer is calculated from the slope of the t-x curve, where $V_a = 1/slope$, then the thickness of each layer is calculated from the velocity values and intercept time, here, the intercept time is the time at offset = 0. The generated simple velocity model is used as the initial velocity model for the traveltime inversion process. The calculated initial velocity values are $314 - 458$ m/s, $556 - 616$ m/s, and $1966 - 2690$ m/s for the first, second and third layer, respectively, while the thicknesses are $2.5 - 8.1$ and $12 - 21$ for the first and second layer, respectively.

The picked traveltimes were inverted to generate a P-wave velocity tomogram. The forward modelling was generated using the finite-difference solution of the ray equations derived from the eikonal equation (Vidale, 1988; Qin et al., 1992). The traveltime inversion was accomplished using the conjugate-gradient approach (Nolet, 1987; Nemeth et al., 1997). A total of 20 iterations were used to invert the traveltimes and the final P-wave tomogram is shown in Figure 11a.

The following observations can be shown on the traveltime tomogram (Figure 11a):

- High-velocity zone located between offset 62 m and 125 m with P-wave velocity values ranging between 350 and 530 m/s and maximum depth of 27 m from ground surface. This zone lies at the center of the crater impact area, here, the increase in the seismic velocity values relative to the surroundings is matching with the (Barton et al., 2010) case study.
- A depression in the contour lines 680 m/s and 1200 m/s (Figure 11a) between offsets 60 m and 112 m, which lies beneath the high-velocity anomaly. This depression could be due to the impact process. The depression of the contour line is equal to 4.3 m and 3.0 m at contour lines 680 m/s and 1200 m/s, respectively.

Three different velocity-depth (v-z) profiles are extracted from the traveltime tomography image (Figure 11b) located at offsets 37 m, 92 m, and 168 m.

- The v-z profile at offset 37 m shows that the velocity of the top layer is almost constant at 300 m/s up to a depth 12.0 m from ground surface, then it shows a high rate of change from 12.0 m to 17.0 m where the velocity increases to 540 m/s, finally a slower rate of change between 17.0 m and 45.0 m where the velocity increases to 1430 m/s.
- The v-z profile at offset 92 m shows that the velocity of the top layer slowly increases from 380 m/s to 470 m/s between depths 4.0 m and 11.0 m. A small high-velocity anomaly of 550 m/s is shown at depth 13.3 m from ground surface, then the velocity increases with variable rate to reach 2270 m/s at a depth of 49 m.
- The v-z profile at offset 168 m shows an almost constant rate of change where the velocity values increase from 300 m/s to 920 m/s between depth 4.0 m and 31.0 m, then the rate of change increases up to a depth of 46.0 m where the velocity reaches 1860 m/s.

3.5 Ground Penetrating Radar (GPR)

To probe the details of the crater morphology twelve profiles covering most of the Philby-B crater was recorded during the first field campaign (Figure 2) using a north-south direction and an expected probing depth of 40 to 60 m below ground surface. A GSSI system is used with two unshielded multi frequency antennas. The peak frequency we selected is 35 MHz to reach a depth of 40 m to 60 m from ground surface. One common mid-point gather is recorded at the site to find the GPR propagation velocity. The reflection event is picked and the GPR velocity is found from the slope of the $t^2 - x^2$ curve where the velocity (v_{GPR}) is given by: $v_{GPR} = \frac{1}{\sqrt{slope}}$. The calculated GPR propagation velocity is 12.3 cm/ns, which is used to convert the recorded GPR data from time to depth. To double check our field measurements and calculations, we calculated the GPR propagation velocity of the direct waves, and we found that it equals to 29.6 cm/ns which is very close to the speed of light.

Three filters are used to enhance the recorded GPR profiles. The first one is a band-pass filter with pass band 15 - 50 MHz, then gain to enhance the amplitudes at later arrivals, and finally a 2D 4X4 running average to decrease any random noises.

Three individual profiles are shown in Figure 12 and has been divided into three regions: a lower low-angle tilted reflector particularly strongly developed towards the southern part of profile 6 and 1 (part C), a middle part horizontal to low angle (part B) and an upper horizontal reflector (part A). The transition between C and B is interpreted as the bottom of the transition crater during formation , whereas the A-B transition represent the transition between fall back and dune sand.

The GPR profiles have been combined into a 3D diagram of the crater shown in Figure 13. The crater is rather flat and slightly asymmetrically

4 Discussion

The current geophysical study shows that the subsurface at the meteorite site can be divided into the following zones. The deeper zone composed of the bedrock of the study area; this bedrock is primarily Sabkha (a coastal, supratidal mudflat or sandflat in which evaporite-saline minerals accumulate as a result of semiarid to arid climate). Usually, the interface between the Sabkha and the overlaying sand-dunes is horizontal, here it is detected at the average elevation of 150 m above mean sea level (MSL as shown in Figure 8). A crest is traced in between the two impact zones (Philby-A and Philby-B, from 110-180 m along the seismic profile shown in Figure 11) at the depth of 35 m from the ground surface. A trough (low) is found to be located between 220-330 m along the seismic profile, and 46 m below the surface of the impact zone of Philby-B. The Sabkha is indicated in blue (Figure 8), in this region the resistivity varies from 1 - 17 Ohm-m. Since the average elevation in the study area is 190 m above MSL and the interface between sand and sabkha found at the average elevation of 150 m, this means that the average thickness of the sand layers is about 40 m.

The green zone (resistivity from 17 - 150 Ohm-m) in Figure (8) represents the undisturbed sand zone and the red zone (with resistivities from 150 - 410 Ohm-m) can be determined as the deformed sand due to the impact of the meteorite in the sand layer. Two main deformed zones are detected on the TEM result (Figure 8). The first one is about 70 meters wide (40-110 m) and related to Philby-A. The second one, is about 110m wide, extended from 210 m - 320 m, and agrees with the location of Philby-B. The depth of the deformed zones are about 32 m and 38 m at Philby-A and Philby-B, respectively. The black zones represent the melt zone, mixed with fragments from the meteorite. The resistivity variation of this zone is much higher (410-1000 Ohm-m) than the surrounding/host materials. A resistivity reversal is also found below Philby-B which is probably related to the melt zone. A big fraction of these melted materials is also found in the southeast area of the study area at the same burial depth (from 350m - 420m along the profile). The location and depth of the melted (high resistivity) material was also verified by the velocity reversal (as high velocity area) depicted at the 2D seismic profile at the depth of 13 m and at 92 m offset from the begging of the seismic profile (Figure 11a and blue line of Figure 11b).

(Roddy et al., 1977; Wynn, 2002a; Wynn & Shoemaker, 1998) suggested that the meteorite would have had to arrive from the N60^{o}W direction at a pitch angle of less than 22^o from the horizontal. Based on the TEM modelling, the pitch angle (interface between the deformed and undisturbed sand) is found to be 24^o from horizontal. This should cause an asymmetry to the impact zone as suggested by other researchers for different impact zones (Roddy et al., 1977). The spatial distribution of the degree of disturbance as shown in Figure 8 and the high resistivity formations (black zones), support the hypothesis that the meteorite stroke the Earth's surface from NW to SE direction that also cause an asymmetry at Philby-B as shown on the GPR profiles (Figure 12).

5 Conclusions

The objective of this work was to apply multi-geophysical approaches to locate the unseen crater (Philby-A) and characterize the exposed crater (Philby-B) estimating their geometrical characteristics, such as diameter and thickness of impact zone. Moreover, the stratigraphy of the study area were depicted into three main units/zones, impact zone, deformed and undisturbed zone. Finally, the geometry/assymetry of the deformed zone gave us evident about the direction of the meteorite's impact.

The low to medium resolution TEM data provided information about the geometry of both craters and the stratigraphy of the study area. A high resistivity anomaly was found from the TEM interpretation which was confirmed by the high-resolution seismic survey. The internal geometry of the Philby-B craters was enhanced by the processing of the acquired high-resolution GPR data. The magnetic data were defined the geometry of the injecta material around the Philby-B crater. The resulted geometry agreed with similar studies in other craters worldwide. Other than that, no high magnetization source (remaining fragment of the meteorite) was found in the broader study area. The above findings were enlightening the post-impact stage.

Several samples were collected during the two expeditions and geochemical as well as thin-sections analysis will be applied in the near-future to reconstruct, if possible, the pre-impact and the interaction (impact mechanism) between the host materials and the meteorite during the impact.

It is proved that multigeophysical approaches can be essential and successful for the exploration of complex study areas. Future geophysical investigations of the Wabar craters may benefit from using airborne EM and magnetic technology to better image the subsurface avoiding levelling problems, having faster coverage of the study area, and combining with accurate positioning the data quality can be maximum.

6 Data Availability Statment

The field data used in this work can be downloaded for free from www.pangaea.de, submission number: PDI-25338, keywords: Seismic, ground-penetrating radar, Wabar.

7 Conflict of Interest

The authors declare no conflict of interest.

8 Acknowledgments

We would like to thank Dr. Abdulaziz Obaid Al-Kaabi for organizing and leading both expeditions. A special thank to Mr. Geraiyan M. Al-Hajri, our guide in both expeditions, for guiding us safely between the sand-dunes of the empty quarter.

References

Abercrombie, T. J. (1966). Saudi Arabia. beyond the sands of Mecca. *National Geographic*, *1291*, 1-53.

Barton, P. J., Grieve, R., Morgan, J. V., Surendra, A., Vermeesch, P., Christeson, G., … Warner, M. (2010). *Seismic images of chicxulub impact melt sheet and comparison with the sudbury structure, in large meteorite impacts and planetary evolution iv (eds r.l. gibson and w.l. reimold).* Geological Society of America, Boulder, CO. doi: https://doi.org/10.1130/2010.2465(07)

Basurah, H. M. (2003). Estimating a new date for the Wabar meteorite impact. *Meteoritics and Planetary Science*, *38*, A155-A156.

Dabboor, M. D., Braun, A., & Kneen, M. A. (2013). Tracking sand dune migration in the Rub Al-Khali with icesat laser altimetry. *International Journal of Remote Sensing*, *34*, 3832-3847.

Durrheim, R. J. (1986). *Recent reflection seismic developments in the witwatersrand basin. in reflection seismology: A global perspective, edited by barazangi m. and brown l.* American Geophysical Union.

Edgell, H. S. (1990). Evolution of the Rub' Al-Khali desert. *Journal of King Abdul Aziz University, Earth Science*, *3*, 109-126.

Edgell, H. S. (2006). *Arabian deserts: Nature, origin and evolution.* Dordrecht, The Netherlands: Springer.

Folco1, L., Martino, M. D., Barkooky, A. E., D'Orazio, M., Lethy, A., Urbini, S., ... Sharkawi, M. E. (2010). The kamil crater in egypt. *Science*, *329*, 804.

Gilder, S. A., Pohl, J., & Eitel, M. (2018). *Magnetic signatures of terrestrial meteorite impact craters: a summary in: Luhr h, wicht j, gilder sa, holschneider m (eds) magnetic fields in the solar system.* Springer.

Gnos, E., Hofmann, B. A., Halawani, M. A., Tarabulsi, Y., Hakeem, M., Shanti, M. A., ... Ramseyer, K. (2013). The Wabar impact craters, Saudi Arabia, revisited. *Meteoritic and Planetary Science*, *48*, 2000-2014.

Grieve, R. A. F. (2006). *Impact structures in Canada.* Geological Association of Canada.

Grieve, R. A. F., & Pilkington, M. (1996). The signature of terrestrial impacts. *AGSO Journal of Australian Geology and Geophysics*, *16*, 399-420.

Henkel, H., & Reimold, W. U. (1998). Integrated geophysical modelling of a giant, complex structure: Anatomy of the vredefort structure, south africa. *Tectonophysics*, *287*, 1-20.

Herndon, J. M., & Rowe, M. W. (1974). Magnetism in meteorites. *Meteoritics*, *9*, 289-305.

Hildebrand, A. R., Penfield, G. T., & Kring, D. A. (1991). A possible Cretaceous-Tertiary boundary impact crater on the Yucatan Peninsula, Mexico. *Geology*, *19*, 867-871.

Jansa, L. F., Pe-Piper, G., Robertson, P. B., & Freidenreich, O. (1989). Montagnais:

A submarine impact structure on the Scotian Shelf, eastern Canada. *Geological Society of America Bulletin*, *101*, 450-463.

McClure, H. A. (1976). Radiocarbon chronology of late quaternary lakes in the arabian desert. *Nature*, *263*, 755-756.

Morgan, J., & Rebolledo-Vieyra, M. (2013). *Impact cratering: Processes and products.* Blackwell Publishing Ltd.

Nemeth, T., Normark, E., & Qin, F. (1997). Dynamic smoothing in crosswell traveltime tomography. *Geophysics*, *62*(1), 168-176.

Neville, A. S., Cook, D. J., Afifi, A. M., & Stewart, S. A. (2014). Five buried crater structures imaged on reflection seismic data in Saudi Arabia. *GeoArabia*, *19*, 17-44.

Nolet, G. (1987). *Seismic tomography: with applications in global seismology and exploration.* Springer Publ. Co.

Osinski, G. R., & Pierazzo, E. (2013). *Impact cratering processes and products.* Wiley - Blackwell Publishing Ltd.

Philby, H. S. B. (1933a). *The empty quarter.* Constable and Co., London.

Philby, H. S. B. (1933b). Rub'al Khali. *Geographical Journal*, *81*, 1-21.

Pilkington, M., & Grieve, R. A. F. (1992). The geophysical signature of terrestrial impact craters. *Reviews of Geophysics*, *30*, 161-181.

Pohl, J., Stoeffler, D., Gall, H., & Ernstson, K. (1977). The Ries impact crater, in impact and explosion cratering: Planetary and terrestrial implications. *Proceedings of the Symposium on Planetary Cratering*.

Prescott, J. R., Robertson, G. B., Shoemaker, C., Shoemaker, E. M., & Wynn, J. (2004). Luminescence dating of the Wabar meteorite craters, Saudi Arabia. *Journal of Geophysical Research*, *109*, 1-8.

Pretorius, D. A., Brink, W. C. J., & Fouche, J. (1986). *Geological map of the witwatersrand basin. in mineral deposits of southern Africa, edited by Anhaeusser C. R. and Maske S.* Geological Society of South Africa.

Qin, F., Luo, Y., Olsen, K. B., Cai, W., & Schuster, G. T. (1992). Finite-difference solution of the eikonal equation along expanding wavefronts. *Geophysics*, *57*, 478-487.

Roddy, D. J., Pepin, R. O., & Merrill, R. B. (1977). *Impact and explosion cratering.* Pergamon Press New York.

Salisbury, H. M., Iuliucci, R., & Long, C. (1994). Velocity and reflection structure of the sudbury structure from laboratory measurements. *Geophysical Research Letters*, *21*, 923-926.

Shoemaker, E. M., & Wynn, J. C. (1997). Geology of the wabar meteorite craters, Saudi Arabia. *28th Annual Lunar and Planetary Science Conference*, *XXVIII*, 1313-1314.

Spencer, L. J. (1933). *Meteorites and fulgurites. appendix in philby (1933a).* Constable and Co., London.

Spencer, L. J., & Hey, H. M. (1933). Meteoritic iron and silica-glass from the meteorite craters of Henbury central Austarlia and Wabar Arabia. *Moneralogical Mgazine*, *23*, 387-404.

Sweeney, J. F. (1978). Gravity study of a great impact. *Journal of Geophysical Research*, *83*, 2809-2815.

Therriault, A. M., Reimold, W. U., & Reid, A. M. (1996). Vredefort granophyre: Field studies. *The South African Journal of Geology*, *99*, 1-21.

Tinker, J., de Wit, M., & Grotzinger, J. (2002). Seismic stratigraphic constraints on neoarchean-paleoproterozoic evolution of the western margin of the kaapvaal craton, south africa. *South African Journal of Geology*, *105*, 107-134.

Tong, C. H., Lana, C., Marangoni, Y. R., & Elis, V. R. (2010). Geolectric evidence for centripetal resurge of impact melt and breccias over central uplift of Araguainha impact structure. *Geology*, *38*, 91-94.

Urbini, S., Nicolosi, I., Zeoli, A., El-Khrephy, S., Lethy, A., Hafez, M., … Folco, L. (2012). Geological and geophysical investigation of kamil crater, Egypt. *Meteoritics and Planetary Science*, *47*, 1842-1868.

Vidale, J. (1988). Finite-difference calculation of travel times. *Bulletin of the Seismological Society of America*, *78*(6), 2062–2076.

Wynn, J. (1996). Mapping Armageddon with a magnetometer - the Wabar impact site at 61^{o}c. *Technical report, US Geological Survey, Reston, VA*, 20192.

Wynn, J. (2002a). Mapping an iron-meteorite site with a magnetometer, and implications for the probability of a catastrophic impact on Earth. *Journal of Environmental and Engineering Geophysics*, *7*, 143-150.

Wynn, J. (2002b). Mapping armageddon with a magnetometer - the Wabar impact site at 61^{o}C. *Journal of Environmental & Engineering Geophysics*. doi: 10

.4133/1.2927080

Wynn, J., & Shoemaker, E. (1998). The day the sands caught fire. *Scientific American - SCI AMER*, *279*, 64-71. doi: 10.1038/scientificamerican1198-64

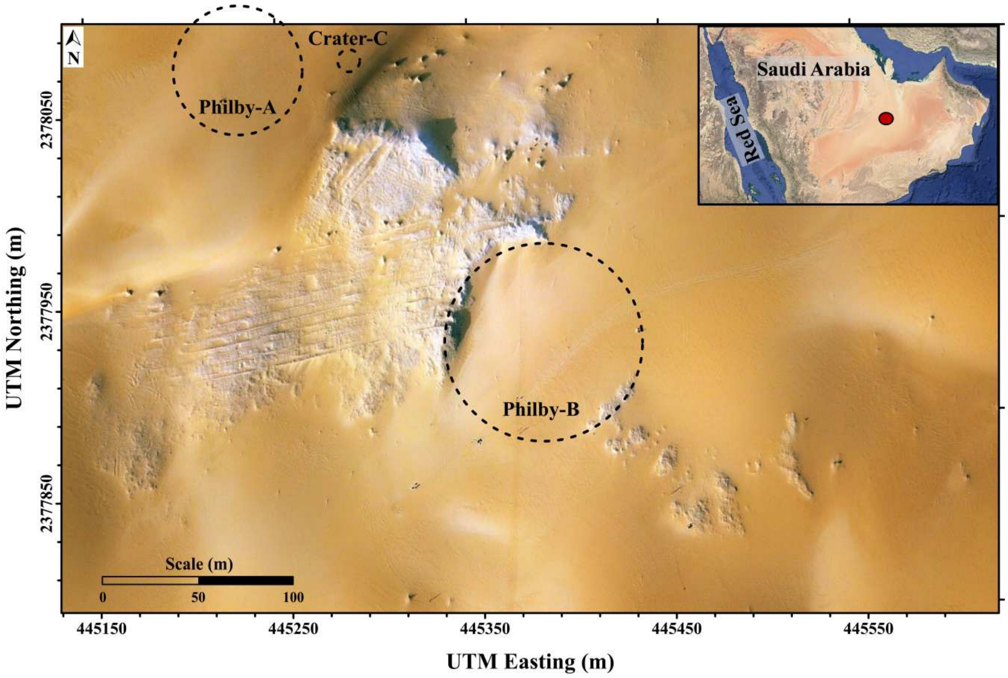

Figure 1. Wabar crater field photographed from drone (date 11 Dec. 2019) with the position, extent and naming of the 3 craters using data of (Gnos et al., 2013). Parallel lines shown to the west of Philby-B crater are tracks from vehicles of former visitors. Insert is a map of Saudi Arabia marking the position of Wabar (red dot).

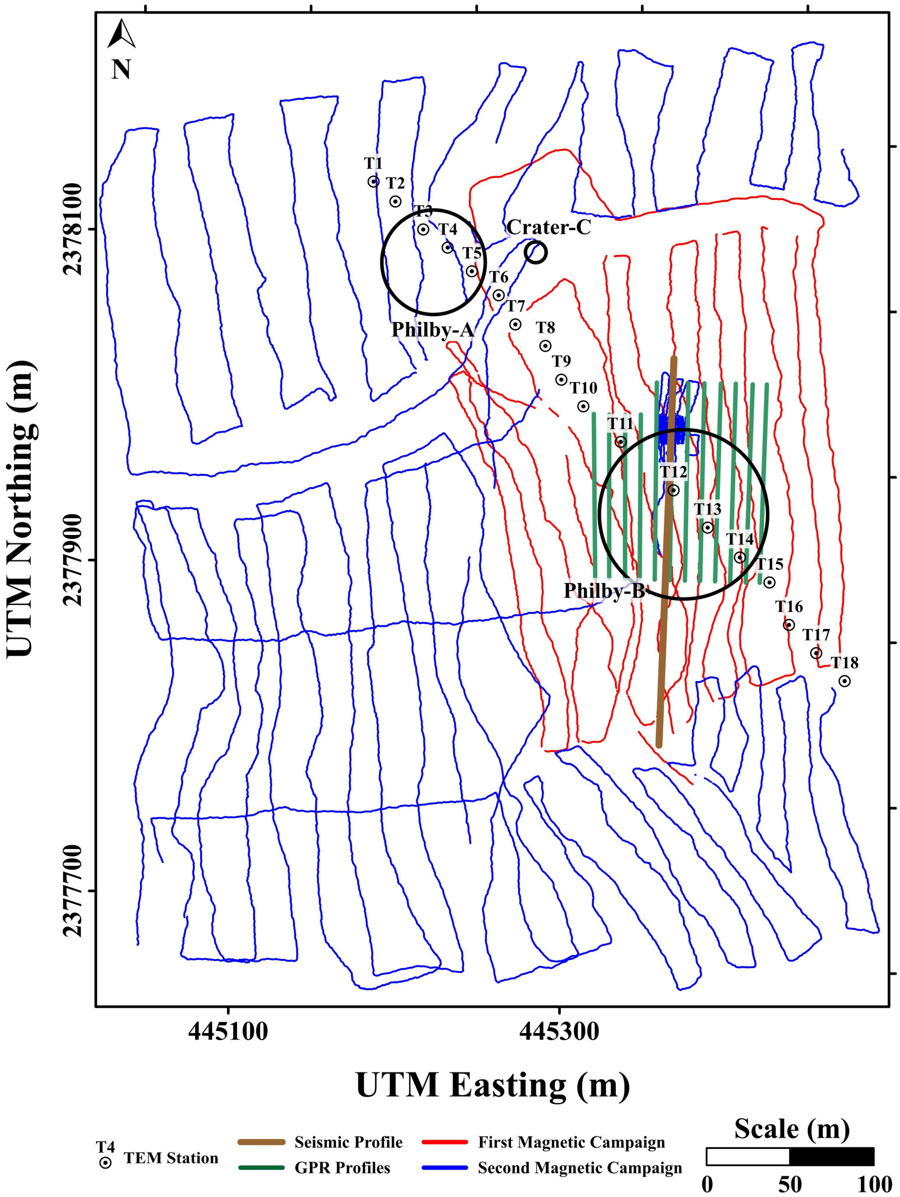

Figure 2. The locations of the recorded geophysical data. Red and blue lines indicate the tracks of magnetic recordings from the first and the second campaign, respectively. Brown line shows the location of the seismic profile, it runs from south to north. The Green lines are the GPR profiles, all of them are running from south to north with the first profile located at the western side and last profile located at the eastern side. T1 to T18 are the locations of the recorded 18 TEM soundings. The three black circles represents the three craters Philby-A, Phibly-B, and Crater-C.

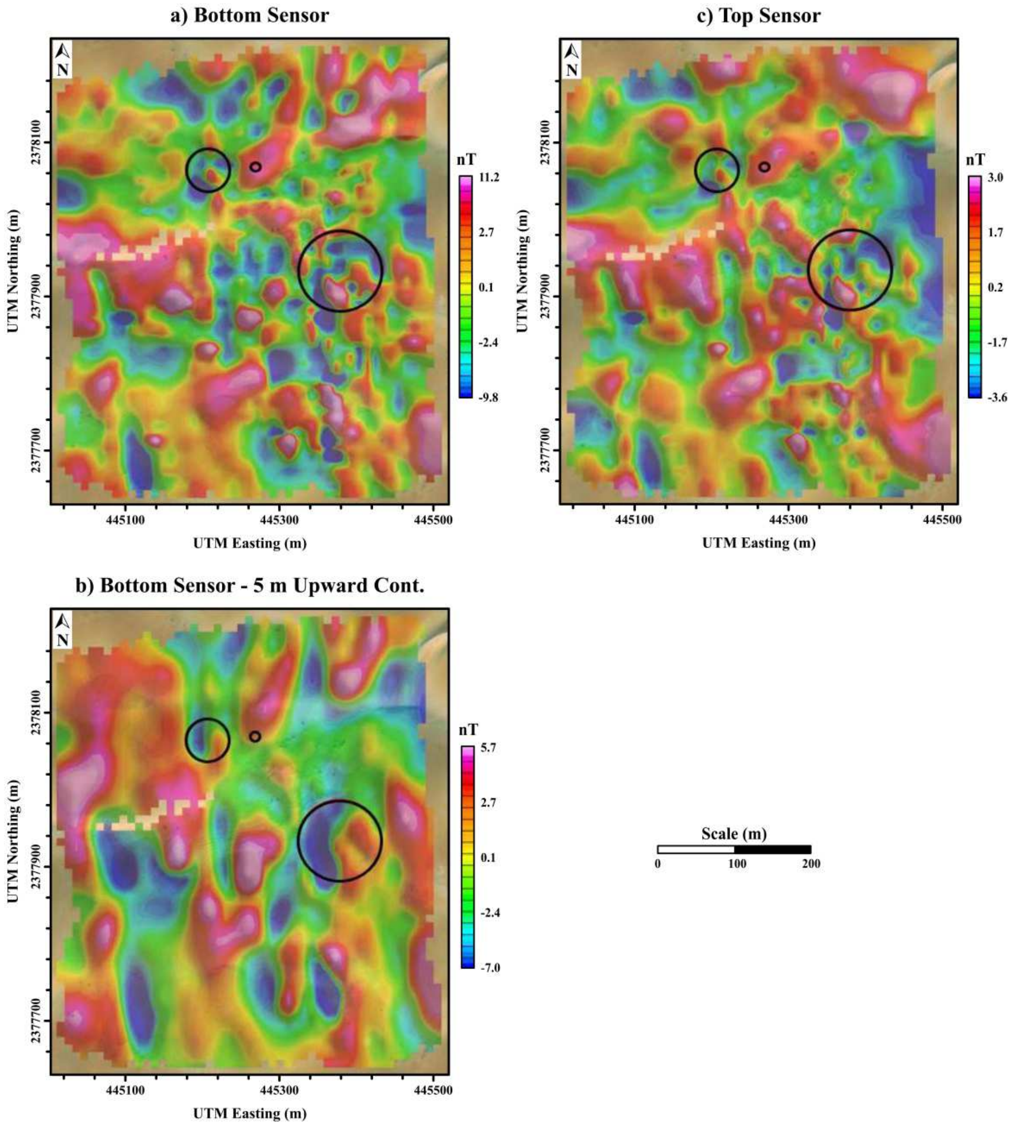

Figure 3. Total magnetic field measured by a) bottom sensor and c) top sensor. b) Shows the bottom sensor after 5 m upwards continuation. Extent of craters are indicated (see Figure 2).

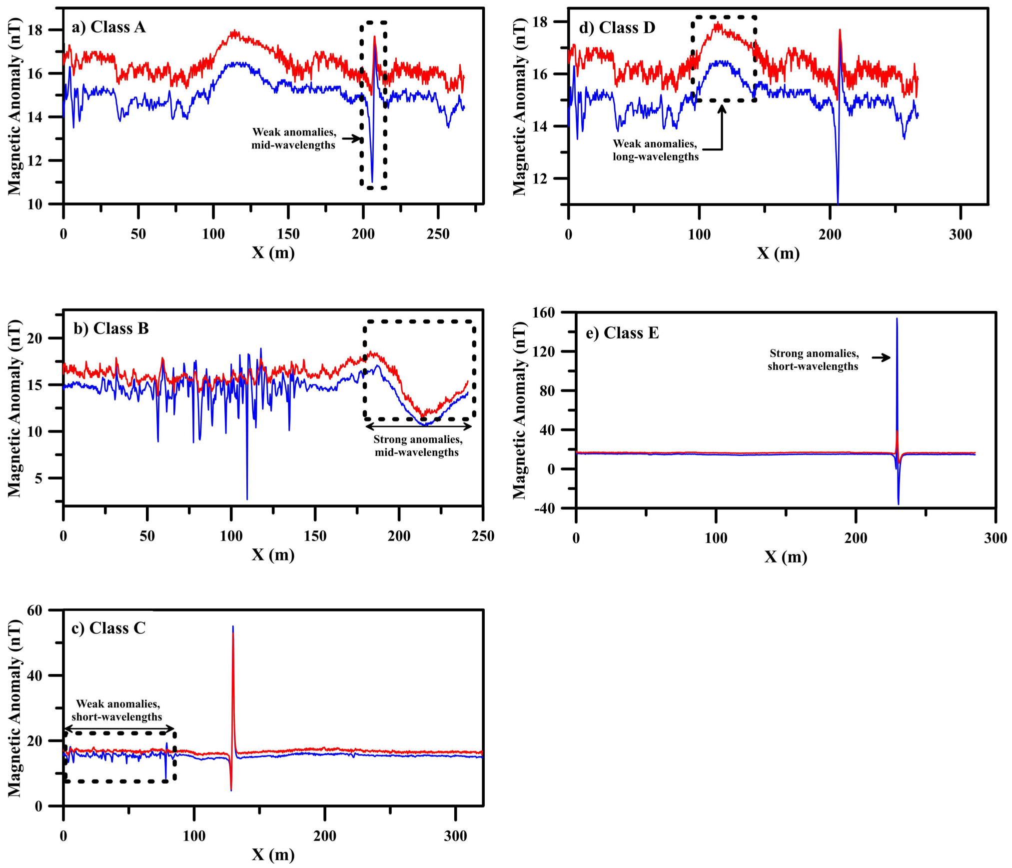

Figure 4. Classification of magnetic data based on amplitude-wavelength analysis, bottom and top sensors are shown as red and blue lines, respectively.

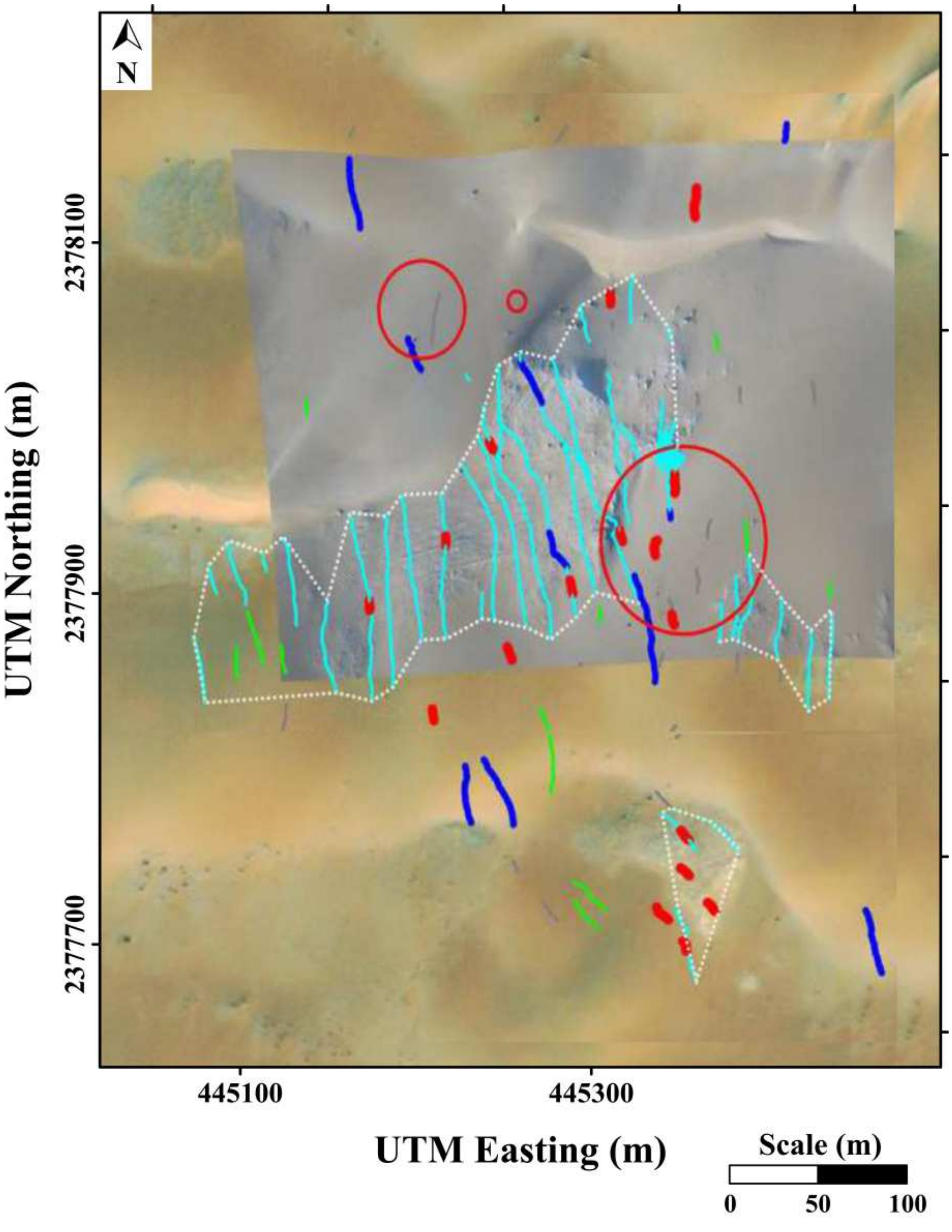

Figure 5. The spatial distribution of the different magnetic types signal as described in Figure 4. Red circles depict the locations of the already known craters. White dotted area indicate abundant class C magnetic signal.

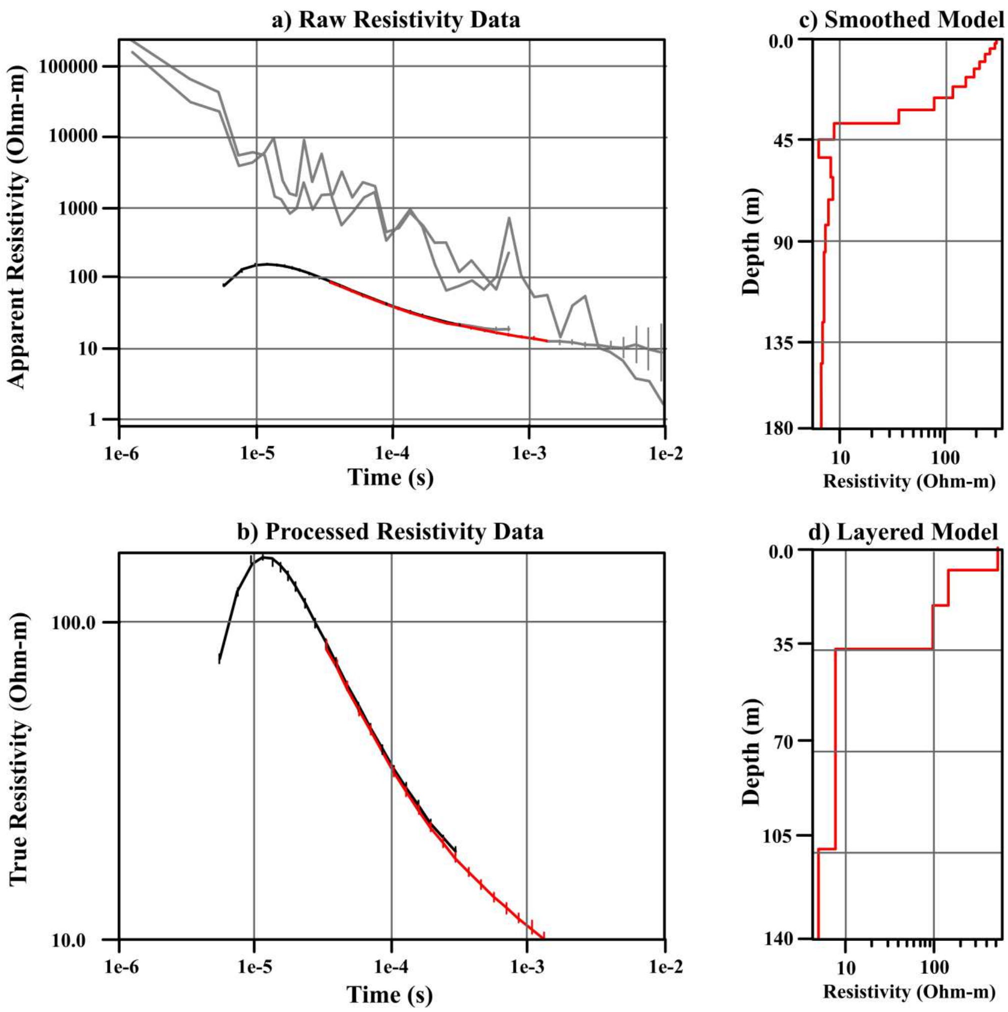

Figure 6. a) The stacked raw, low (green line) and high (purple line), Rho (Ohm.m) data for T1 are shown. Data with high error bars or close to noise level (grey lines on the top of a) are excluded. b) Final TEM data from both moments, are inverted. Green and purple error bars shown the calculated data and the continuous lines show the observed data. c and d) The inverted smooth (c) and layered (d) final resistivity models.

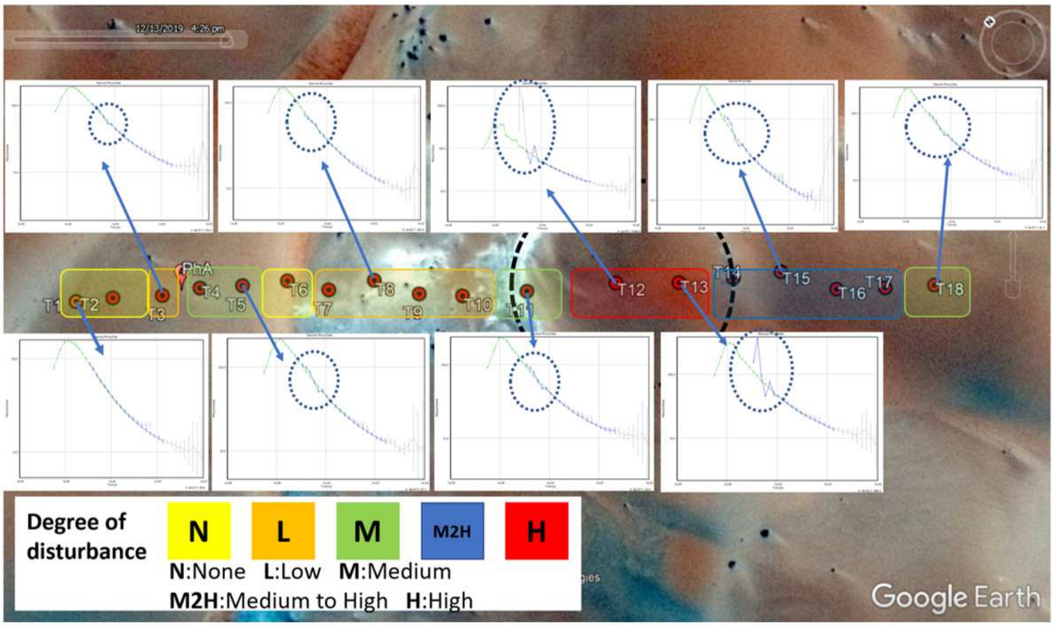

Figure 7. Qualitative interpretation of TEM soundings. The locations and the names of the TEM soundings are shown with the red dots (T1-T18). The perimeter of the Philby-B is shown by dashed thick black circle.

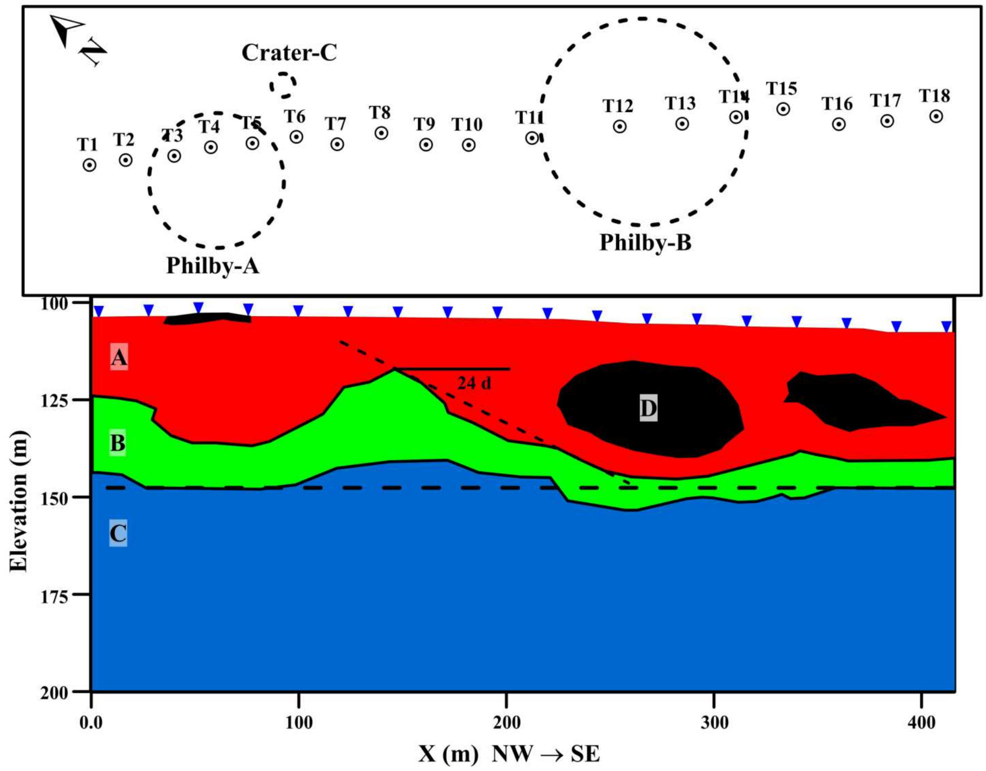

Figure 8. (Bottom) A quasi-2D geoelectrical section of the processed TEM soundings (T1 to T18) along the NW-SE profile. (Top) The location of both craters, Philby-A (between T4 and T5) and Philby-B.

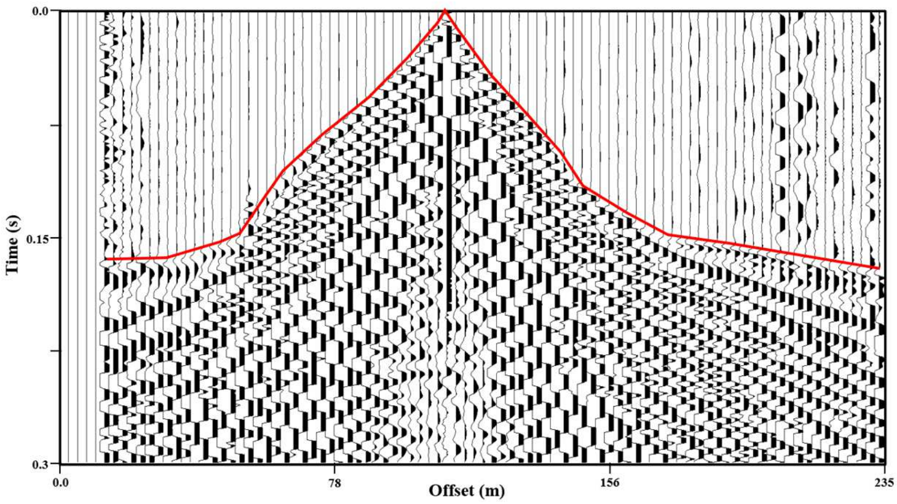

Figure 9. Example of the recorded traces. This figure shows the common receiver gather no. 24 where the red line marks the picked first break travetimes.

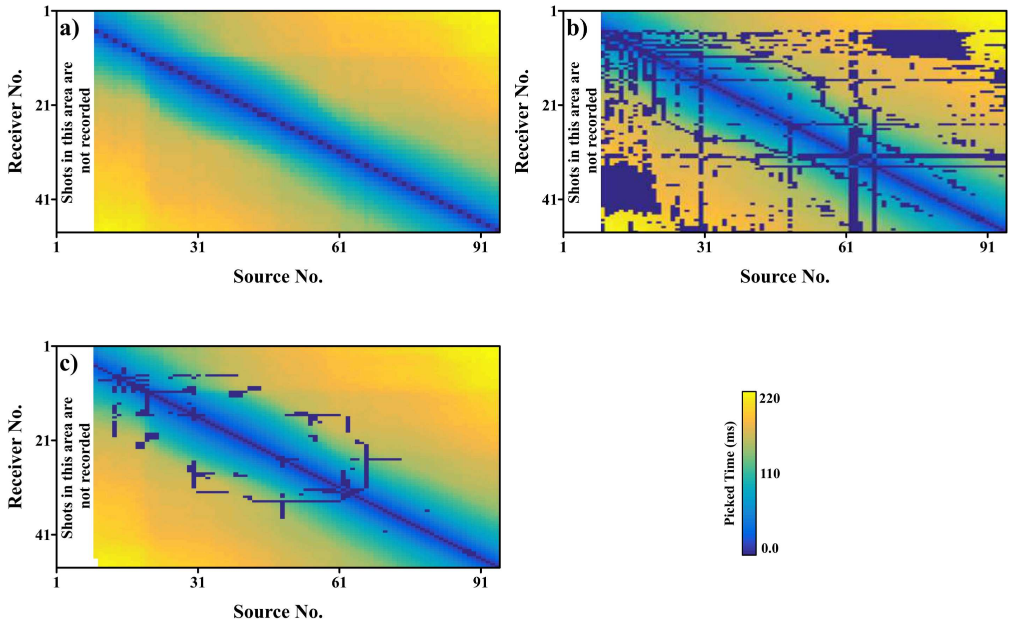

Figure 10. The result of the reciprocity test. a) Raw traveltime picking, b) after running the reciprocity test, here, dark blue colors show the rejected traveltimes (24% of the total picks), and c) after repicking the rejected traces, some traces still did not pass the reciprocity test (3.8%), so they are permanently rejected and not included in the traveltime inversion process.

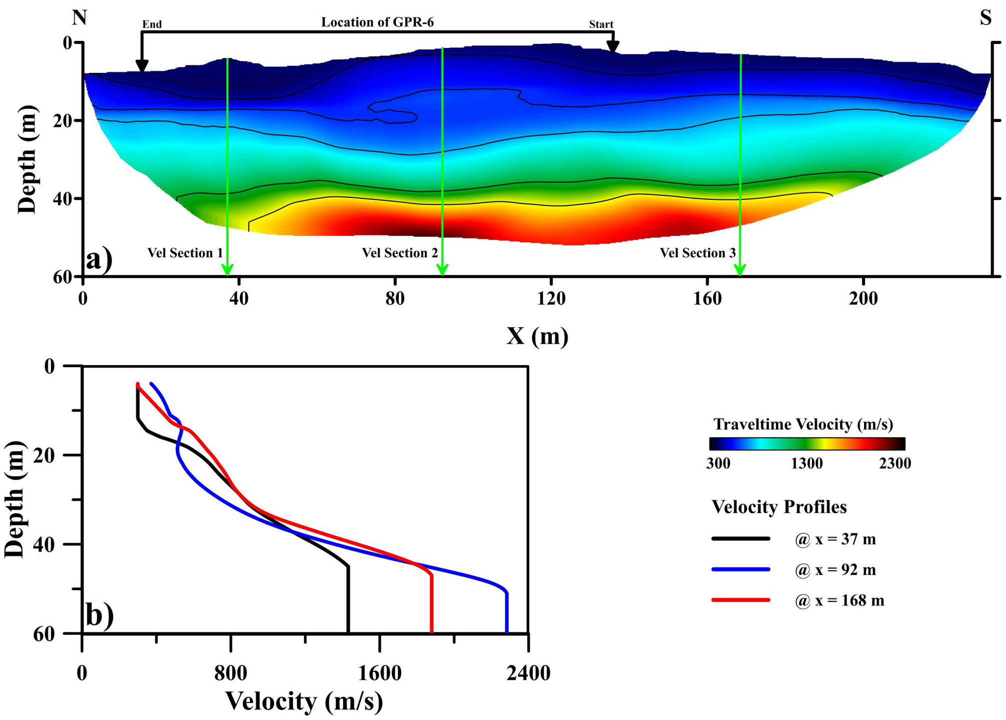

Figure 11. a) The traveltime tomogram after 20 iterations. The location of GPR profile no. 6 is shown as black line. b) Three velocity-depth profiles, green lines in a), extracted from the traveltime tomogram and located at offsets 37 m, 92 m, and 168 m.

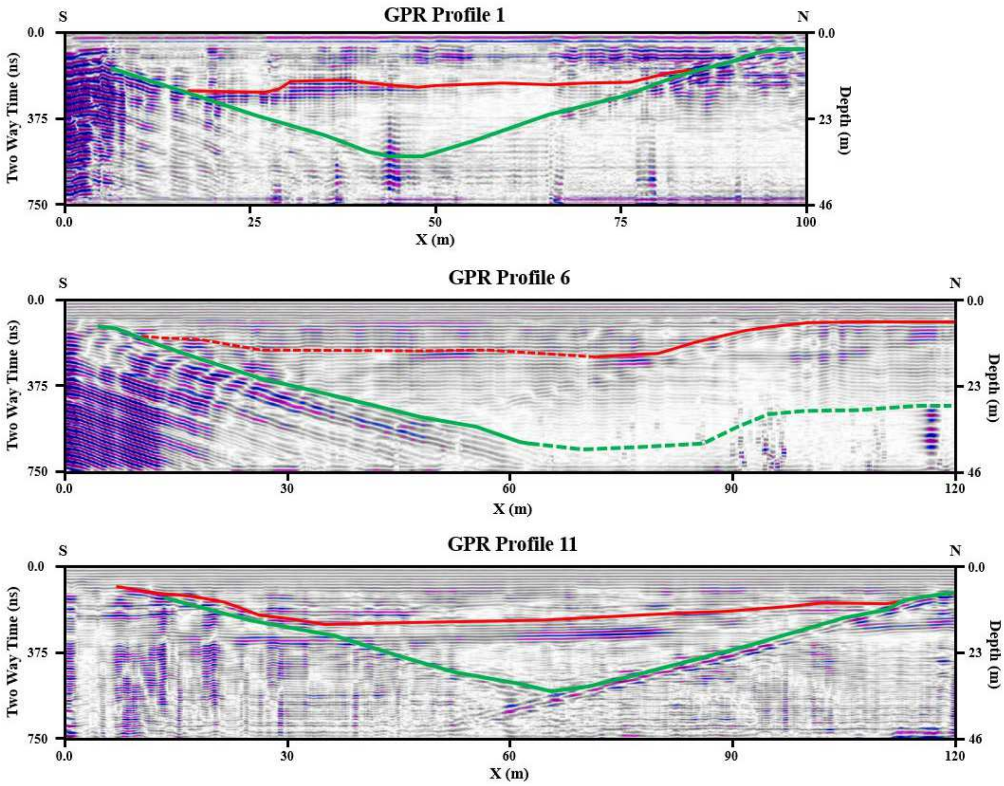

Figure 12. GPR profiles 1, 6, and 11 after processing and interpretation. Red line shows the boundary between the first and the second layers while the green line shows the bottom of the crater impact. Dashed lines (red or green) indicates expected (interpolated) location.

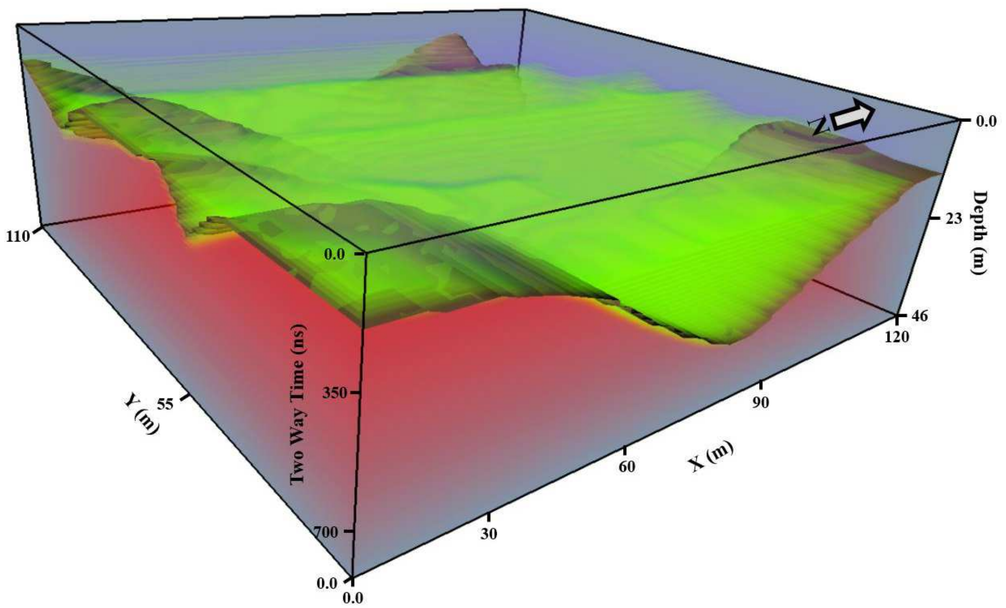

Figure 13. A 3D cube constructed from all recorded GPR profiles. Green color indicates the bottom crater impact as interpreted from the GPR profiles. The cube covers the Philby-B site.

Appendix A Historical Background

The small-scale Wabar impact crater field in Rub Al-Khali is rare among these because of the co-occurrence of impactor and crater(s) (a characteristic shared with other craters, and unique by its setting within an active sand dune field (Philby, 1933a, 1933b). The fall is fairly recent, yet we have traced no traditional legend among the (local) Bedouins neither to the origin of the iron at the site nor to the origin of the craters, implying that the latter stages of the fall was unwitnessed. The occurrence of metallic iron at the site, however, was recognized and reflected in naming of the site as Al-Hadida (Arabic translating to place of Iron). As such, the site was known long before the visit of Philby's expedition in 1932, and modest sized pieces, carried by camel, had been transported to other places being worked and used for utensils such as camel charm or traded as-found (two meteorites formerly known as Nejed I and II, but now believed to be fragments of the Wabar meteorite, were acquired by the British Museum in the 1930s). A rather large piece of the meteorite was known to members of the Philby expedition (having the size comparable to a camel hump) but could not be located in 1932. The camel hump-sized piece was revealed again in the 1960's and recovered by vehicle in 1965 (Abercrombie, 1966). No significantly sized meteorite pieces have been recovered later from the site.

A major purpose of Philby's expedition was to track the site of a legendary city called Wabar or Ubar (in different transliterations). From the descriptions in (Philby, 1933a) it is evident that Philby himself immediately upon arrival at the site realized that the site was not at all related to the city he sought. Philby measured and mapped the craters and the distribution of slags, and collected samples that upon arrival to the British Museum in London allowed Spencer in 1933 to identify the craters as meteorite impact craters by identifying one sample as a fragment of an iron meteorite and the other samples as glasses resulting from the impacts (Spencer, 1933; Spencer & Hey, 1933).

Current information on the site is based on field work carried out by Philby in 1932, the Zahir expeditions in 1994 and 1995 (Wynn & Shoemaker, 1998; Wynn, 2002b) and more recently by an expedition in 2008 reported by Gnos et al. (2013). As summarized in Gnos et al. (2013) the meteorite is an iron meteorite of group IIIAB. The meteoroid broke up rather late during the fall and the most energetic pieces created the craters. The crater field features 3 almost circular craters having crater rim diameters of 114, 64, and 11 m and designated Philby-B, Philby-A, and 11-m crater, respectively (Figure 1).

In this work we called the 11-m crater as crater C. The distribution of recorded meteorite recovery site and craters imply a fall having an incoming direction from the north. The material produced in the impact encompasses a shock-lithified dune sand and glasses being mixtures of sand and oxidized meteorite. Two lines of evidence both indicate a very young fall. Using luminescence techniques, Prescott et al. (2004) found the age of the impact to be 290 ± 38 years BP. This age is in line with a written source reporting a fall on the first of September AD1704 based on observation of a bright fireball in Tarim, Yemen (Basurah, 2003).

One of the major obstacles in investigating the crater field is the active sand dunes, the major causes for dune migration are the wind regime and the type of dunes (e.g., grain size and vegetation cover). (Dabboor et al., 2013) used phase differences method to estimate dune displacement vectors with an accuracy of 5 m root mean square. (Gnos et al., 2013) estimated a maximum depth of the craters as 15 m and an average dune sand thickness of 20-30 m at the site, implying that all the sediment material worked up in the impact is originating from the dune sand. However, ejecta samples commonly feature rounded, light sand grains of several mm in diameter indicating that other sediment sources may have contributed in addition to the dune sand.

Appendix B Geological Background

Saudi Arabia is known for its dune deserts, one of the largest in the world. Still, most importantly, the Empty Quarter (EQ) is the world's largest continuous sand desert area covering an area of about 650.000 km^2. EQ is located in the South-East part of the Arabian Peninsula, including parts of Saudi Arabia, Oman, the United Arab Emirates, and Yemen.

The EQ desert is part of Rub Al-Khali basin (RaKb), which is geologically bounded by the central Arabian arch in the north, the Oman thrust zone in the east, the Northern Hadramaut arch in the south and the Arabian Shield in the west. The RaKb was formed during Proterozoic time, and its stratigraphic sequence includes various cycles of deposition of clastic and carbonate sediments with local unconformities. During the late Paleozoic and Mesozoic periods, various source rock formations, reservoirs and seals were formed at different levels. The Oman thrust zone and its compression phase, formed the traps in the broader area. The RaKb was covered with sands, silts, clays, and conglomerates deposited in dunes and sabkhas (a formation rich in clays and evaporite).

In the beginning of the Middle Pleistocene in Saudi Arabia, low dunes began to accumulate in the Rub Al-Khali during arid climatic condition (Edgell, 1990). Linear dunes, having several hundred kilometres long and as much as 200 m high, are the dominant types of dunes in the Rub Al-Khali. Also, star dunes having pyramidal morphology and sinuous radiating arms and up to 300 m high, occur in the southern part of the Rub Al-Khali (Edgell, 2006). Calcareous, and often fossiliferous, marls, and muddy lake deposits, which were dated by radiocarbon to last 800 years, formed in wide spread areal extent between the dunes during the torrential rainfall (McClure, 1976).

During the current survey, the field crew conducted the geophysical survey at Al Hadida site, in Wabar craters (lat 21.503427, long 50.472181) in RaKb. Shoemaker and Wynn (1997) reported that the craters have been formed entirely in the loose sand layer of the RaKb (Figure 1). No bedrock was found in the vicinity of the craters and no bedrock fragments occur in the ejecta from the craters. The sides of the craters were covered with a breccia composed of clasts of shock-compressed sand, known as instant rock. The exposed rim of Phily-B is mantled with bombs and lapilli of black and white slaggy impactite glass and with large and small clasts of instant rock (Figure B1a and b). In places,

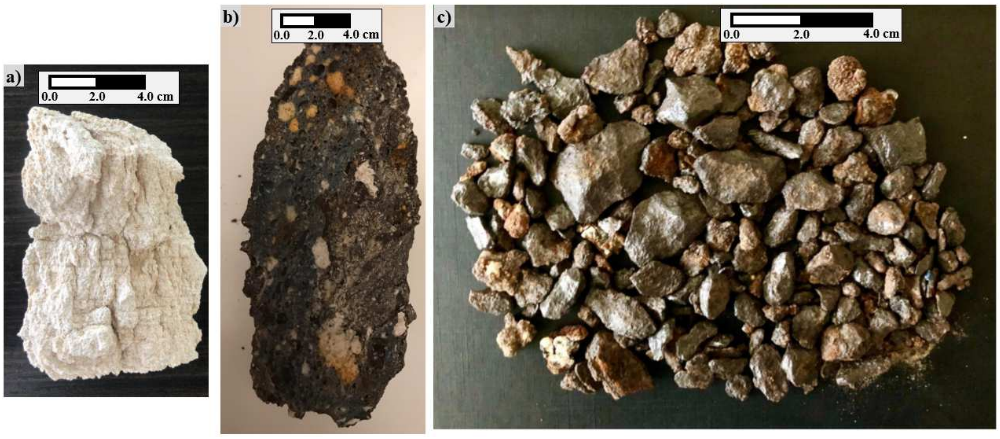

Figure B1. a) A sample of white instant rock. b) White instant rock and Iron-Ni inclusions in black glass. c) Abundant small fragments of meteorites collected from the site.

the white instant rock was found as inclusion in black glass (Figure B1a). Finally, during the expedition, rusty fragments of the iron-nickel meteorite were found (Figure B1c).

(Shoemaker & Wynn, 1997) opened a trench in the study area to obtain information about the deformation of the pre-crater sand deposit. Bedding in the pre-crater sand is upturned in the southern wall of the rim were observed. Outward dips become steeper toward the center of the crater, reaching a maximum of 50 deg. Small thrust micro-faults dipping both toward and away from the crater were detected outside the zone of sharp upturning of the beds.